Chinese Chemical Letters 34 (2023) 108448

Contents lists available at ScienceDirect

Chinese Chemical Letters

journal homepage: www.elsevier.com/locate/cclet

Impact of regio-isomeric monochlorinated end groups on packing mode, miscibility, and photovoltaic performance of asymmetric selenophene-fused M-series acceptors

Ruochuan Liao[a,c], Changquan Tang[a], Yunlong Ma[a], Qingdong Zheng[a,b,*]

[a] State Key Laboratory of Structural Chemistry, Fujian Institute of Research on the Structure of Matter, Chinese Academy of Sciences, Fuzhou 350002, China
[b] State Key Laboratory of Coordination Chemistry, College of Engineering and Applied Sciences, Nanjing University, Nanjing 210023, China
[c] University of Chinese Academy of Sciences, Beijing 100049, China

ARTICLE INFO

Article history:
Received 31 January 2023
Revised 9 April 2023
Accepted 11 April 2023
Available online 13 April 2023

Keywords:
Organic solar cells
Miscibility
Noncovalent interaction
Chlorinated isomers
Molecular packing

ABSTRACT

Optimal bulk-heterojunction (BHJ) morphology is crucial for efficient charge transport and good photovoltaic performance in organic solar cells (OSCs). Yet, the correlation between chemical structures of non-fullerene acceptors (NFAs) and molecular interaction in the BHJ blends remains opaque. Herein, we study three isomeric NFAs referred to as MQ1-x (x = β, γ, or δ) that shared an asymmetric selenophene-fused heteroheptacene backbone end-capped by two monochlorinated end groups. Remarkably, miscibility between the polymer donor of PM6 and MQ1-x successively elevates as the chlorine atoms move from β-, to γ-, to δ-position of terminals. Combined with the varied molecular crystallinity of these NFAs, diverse BHJ morphologies are observed in their blend films. As a result, the MQ1-δ-based devices present the highest PCE of 12.08% owing to the efficient charge dissociation and transport induced by the compact molecular packing and optimal BHJ morphology. Our investigation provides a new insight in the material design that has a good balance in molecular packing and film morphology for high-performance OSCs.

Solution-processed bulk-heterojunction (BHJ) organic solar cells (OSCs) are recognized as good candidates for portable applications compared to conventional silicon-based counterparts owing to their unique merits such as good flexibility, translucent potential, and light-weight nature [1–3]. Nowadays, acceptor-donor-acceptor (A-D-A)-type non-fullerene acceptors (NFAs) with three-dimensional (3D) packing networks and anisotropic charge transport properties have been widely researched for OSCs, which rekindled a new round of passion for the investigation on renewable energy conversion technology over the past decade [4–7]. Generally, A-D-A-type NFAs are composed of three independently tuneable modules: an electron-donating π-conjugated core (D unit), a pair of electron-withdrawing end groups (A units), and sets of side chains, leading to both the structural diversity and self-assembly complexity of the NFAs. With enormous efforts on the A-D-A-type NFAs, power conversion efficiencies (PCEs) of OSCs have exceeded 17% and some even reached 19% [8–13].

The precise control of the molecular configuration of NFAs would strongly affect molecular aggregation behaviors, optoelectronic properties as well as related photovoltaic responses [13–17]. Initially, NFAs featuring IDT/IDTT cores contain both suitable solubility and crystallinity thanks to the side chains on sp^3-hydridized-carbons that remarkably prevent the over-aggregation of the large conjugated skeletons [18]. However, the large steric hindrance of the side chains also prevents the effective π-orbital overlap between neighboring NFA molecules, resulting in monotonous intermolecular interaction and vulnerable stacking networks [19,20]. Therefore, side chains on sp^2-hydridized-nitrogens were incorporated into NFAs, which boost the development of ladder-type fused ring cores readily to self-assemble and in turn endowing outstanding light-harvesting capacities, charge-transport abilities, and photovoltaic performance of the related NFAs, such as M36, MQ6, Y6, and L8-BO [21–24]. The minimized steric hindrance of side chains on the sp^2-hydridized-nitrogens gives BDTPT-type (M-series) and BTP-type (Y6-family) NFAs more freedom in fabricating intricate 3D packing networks with aid of “A to A”, “D to A” or “D to D” π-π interactions [25–28]. Furthermore, NFAs with asymmetric selenophene-fused central π-backbone showed enhanced molecular interaction with increased dipole moment in comparison with the symmetric counterparts [22,29].

* Corresponding author at: State Key Laboratory of Structural Chemistry, Fujian Institute of Research on the Structure of Matter, Chinese Academy of Sciences, Fuzhou 350002, China.
E-mail address: qingdongzheng@fjirsm.ac.cn (Q. Zheng).

https://doi.org/10.1016/j.cclet.2023.108448
1001-8417/

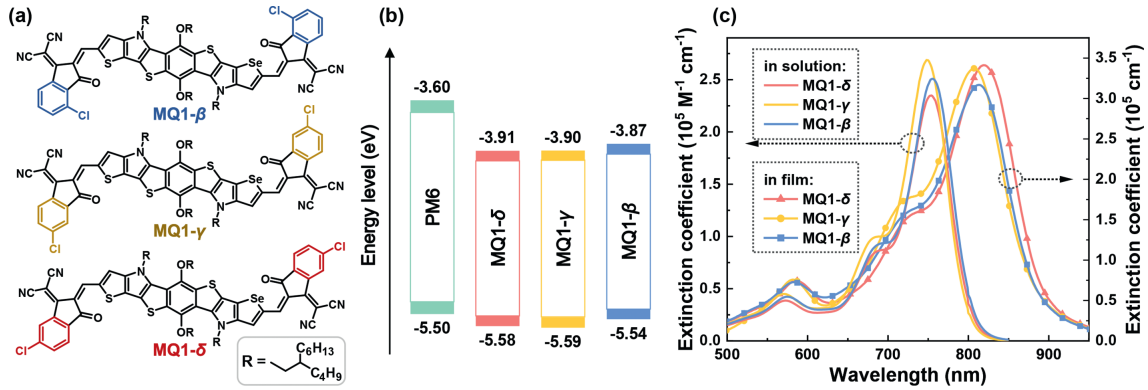

Fig. 1. (a) Chemical structures of MQ1-β, MQ1-γ, and MQ1-δ. (b) CV-derived frontier molecular orbital (FMO) energetics of active layer materials applied in this work. (c) Linear absorption spectra in chloroform solution and solid film of MQ1-β, MQ1-γ, and MQ1-δ.

Multiform molecular packing modes and noncovalent interactions induced by end groups lie at the heart of the long-range order and anisotropic charge transport channels of NFAs [13,30–32]. Typically, halogenated 1,1-dicyanomethylene-3-indanone (IC) end groups were frequently applied to dictate the self-assembly of NFAs, which are driven by diverse noncovalent interaction, including hydrogen bonds (*e.g.*, CN···H, CO···H, F···H, and Cl···H interaction), π-π stacking, S···F, or Cl···O/Cl interaction [5,27,33,34]. Therefore, studies on halogenated end groups are significant in comprehending the relative molecular interaction and photovoltaic performances of NFAs. For instance, Marks *et al.* developed two isomeric NFAs with the π-extension and fluorination strategies, promoting "π-face-to-face" packing and achieving a PCE of 10.3% [35]. In addition, Zhan *et al.* reported a series of NFAs with varied fluorinated IC end groups. Among these acceptors, the tetra-fluorinated NFA (INIC3) exhibited the best crystallinity in BHJ morphology and afforded a PCE of 11.5% [36]. Previous studies on terminal-mediated NFAs mainly focus on the crystallinity of NFAs and seldom on the impact of terminal groups on the miscibility between donors and acceptors. In fact, halogen atoms anchored in the conjugated skeletons would affect the surface energy of organic compounds thereby leading to the varied miscibility with other components [37]. Especially, chlorine atoms in end groups could notably tune the electron density, non-covalent interaction, and crystallinity of NFAs owing to their great electron affinity [6,38]. Hence, the investigation on how chlorinated-end-group-mediated packing affects crystallinity, D/A miscibility, and optoelectronic properties of NFAs merits attention.

In this work, we report three isomer-free dichlorinated NFAs with the same asymmetric selenophene-fused backbone (T-BDTP-Se) yet exhibiting varied molecular aggregation behaviors by altering the chlorine position in the end groups, namely, MQ1-β, MQ1-γ, and MQ1-δ. The change in the chlorine substitute position of terminals induces fine control of molecular aggregation, even in the complex BHJ blends. Intriguingly, the D/A miscibility of NFA with polymer donor PM6 increases as the chlorine substitute changes from β-, to γ-, to δ-position of terminal benzene rings, leading to diverse BHJ blends. In detail, the MQ1-γ-based OSCs outperform the MQ1-β-based counterparts in photovoltaic performance due to the compact molecular packing and better D/A miscibility of MQ1-γ. Remarkably, both compact molecular packing and intermingled BHJ blend of PM6:MQ1-δ guarantee well-balanced carrier transport in the MQ1-δ-based devices thereby leading to its highest PCE of 12.08%.

The synthetic details of MQ1-β, MQ1-γ, and MQ1-δ are displayed in Scheme S1 (Supporting information). As the chlorine changes from β-, to γ-, and to δ-position, the solubility of the related IC end group (IC-Cl-β, IC-Cl-γ, and IC-Cl-δ) in dichloromethane sequentially increases from 16 mg/mL, to 26 mg/mL, and to 130 mg/mL. This result implied that the tendency to crystallization of IC-Cl-β, IC-Cl-γ, and IC-Cl-δ was successively decreased. The varied noncovalent interaction of the three end groups could be ascribed to the resonance effects of chlorine located in different positions of the end groups (Fig. S1 in Supporting information). Specifically, the Cl···O interaction in IC-Cl-β may be responsible for its strongest inclination to self-aggregation, which could partly persevere to corresponding NFAs. Moreover, as depicted in Fig. 1a, the three isomeric small molecules share identical selenophene-containing asymmetric heptacene central π-core anchored by four sets of branched (2-butyloctyl) side-chains. MQ1-β, MQ1-γ, and MQ1-δ were obtained *via* Knoevenagel condensation reactions between the corresponding monochlorinated end groups and the corresponding aldehyde intermediate reported in our previous work [22], with yields of 84%, 91%, and 88%, respectively. The three acceptors were characterized by ^{1}H NMR, ^{13}C NMR, elemental analysis, and high-resolution mass spectrometry (Supporting information).

To evaluate the energy levels of the three acceptors, cyclic voltammetry (CV) and ultraviolet photo-electron spectroscopy (UPS) experiments were performed. As depicted in Fig. 1b and Table 1, energy levels of MQ1-γ and MQ1-δ obtained from the CV measurement are obviously deeper than those of MQ1-β. Similarly, based on the UPS spectra (Fig. S2 in Supporting information), the LUMO/HOMO of MQ1-γ (-4.15/-5.55 eV) and MQ1-δ (-4.17/-5.55 eV) are also deeper than those of MQ1-β (-4.12/-5.51 eV), which is consistent with the energy level trend from the CV results. UV–vis absorption spectra of the three NFAs were shown in Fig. 1c, and the relevant data are summarized in Table 1. In the CF solution (5×10^{-6} mol/L), the maximum absorption peaks of MQ1-β (755 nm) and MQ1-δ (754 nm) were slightly red-shifted than the counterpart of MQ1-γ (748 nm). This may come from the diverse intramolecular S/Se···O interaction related to the carboxylic oxygen of A units, which are vulnerable to the resonance effect of β/δ-chlorine in the benzene rings (Fig. S1). According to the resonance analysis (Supporting information), the intramolecular Cl···O interaction (*ca.* 3.10 Å) induced by charge polarization between β-chlorine and carboxylic group may account for the higher ε_{max} of MQ1-β (2.51×10^5 L mol^{-1} cm^{-1}) in comparison with MQ1-δ (2.35×10^5 L mol^{-1} cm^{-1}). Owing to intense molecular aggregation in solid film, the film state absorption maxima (λ_{max}) of MQ1-β (813 nm), MQ1-γ (807 nm), and MQ1-δ (819 nm) are conspicuously red-shifted than their solution state counterparts (Fig. 1c). The optical bandgap of MQ1-β, MQ1-γ, and MQ1-δ are 1.39, 1.40, and 1.38 eV, respectively, which are calculated from the λ_{onset} edges in thin films (889 nm for MQ1-β, 883 nm for MQ1-γ, and 896 nm for MQ1-δ), respectively (Fig. 1c).

Table 1
Photophysical and electrochemical parameters of the nonfullerene acceptors.

Acceptors	ε_{max}^{sol} ($L mol^{-1}$ cm^{-1})	λ_{max}^{sol} (nm)	λ_{max}^{film} (nm)	E_g^{opt} (eV)[a]	$E_{LUMO/HOMO}$ (eV)[b]
MQ1-δ	2.35×10^5	754	819	1.38	−3.91/−5.58
MQ1-γ	2.69×10^5	748	807	1.40	−3.90/−5.59
MQ1-β	2.51×10^5	755	813	1.39	−3.87/−5.54

[a] $E_g^{opt} = 1240/\lambda_{onset}^{film}$.
[b] HOMO/LUMO energy levels were obtained from CV measurements.

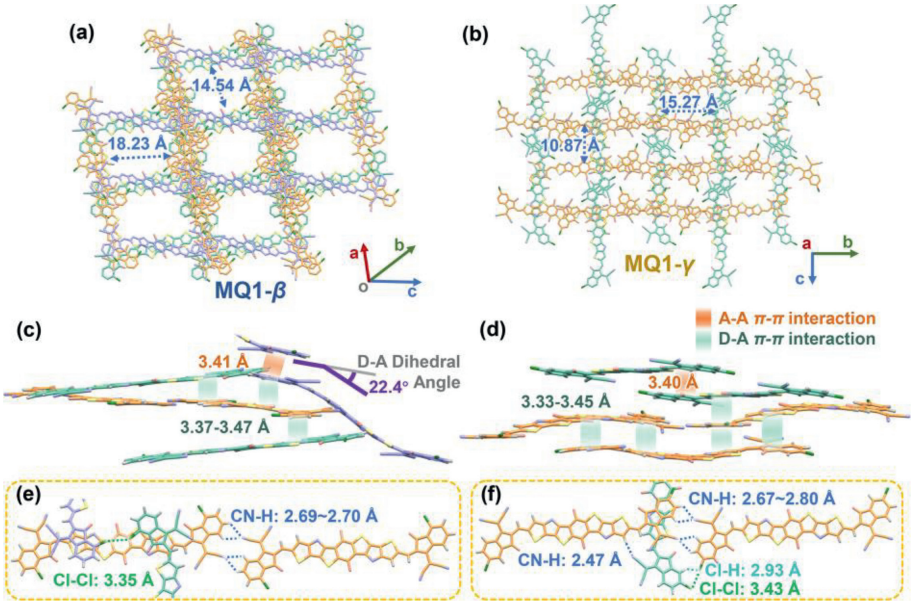

Fig. 2. Single crystal structures and packing modes diagrams. The 3D interpenetrating networks of MQ1-β (a) and MQ1-γ (b). The stacking modes and noncovalent interaction distance of MQ1-β (c) and MQ1-γ (d) from the side view of π-face-on perspective. The noncovalent interaction diagrams about the similar dimer and adjacent molecules of MQ1-β (e) and MQ1-γ (f) from the π-face-on perspective. Alkyl chains are omitted for ease of viewing.

Moreover, the absorption coefficient of MQ1-δ-based film (ε_{max} of 3.41×10^5 cm^{-1}), is larger than those of MQ1-β- (3.15×10^5 cm^{-1}) and MQ1-γ-based films (3.37×10^5 cm^{-1}), which could be due to the more compact molecular stacking for the MQ1-δ-based film.

The polymer of PM6 (Fig. S2) with a wide bandgap was selected as the donor material for fabricating photovoltaic devices. In addition, λ_{onset} edges of the PM6:MQ1-β, PM6:MQ1-γ, and PM6:MQ1-δ blend films are 870, 868 and 882 nm, respectively (Fig. S2). The light-harvesting trend in pristine films of the three acceptors was consistent with those in blend films, indicating that MQ1-δ can capture more photons in both pristine and blend films, which is one of prerequisites for good photovoltaic responses.

Diffraction quality crystals of MQ1-β and MQ1-γ (CCDC Nos. 2213581 and 2213582) were cultured by liquid-liquid diffusion method using toluene as a good solvent, tetrahydrofuran as a buffer-layer solvent, and methanol as a poor solvent. The single crystal X-ray diffraction results (Fig. S3 in Supporting information) indicate that both MQ1-β and MQ1-γ share the slightly twisted configuration interlocked by S/Se···O intramolecular interaction. Specifically, owing to intramolecular Cl···O interaction ($D_{Cl\text{-}O} = 3.10$ Å), MQ1-β possesses smaller $D_{S/Se\text{-}O}$ (2.60 Å) than those of MQ1-γ (2.64 Å). These strong intramolecular interactions may partially account for the conspicuously red-shifted absorption peak of the MQ1-β solution compared to the two other isomeric acceptors. Nonetheless, MQ1-β exhibits worse molecular planarity than MQ1-γ owing to the greater absolute value of the D-A torsion (φ) of MQ1-β (12.7°) than that of MQ1-γ (8.2°). Furthermore, the single-crystal packing diagrams were systematically investigated and presented in Fig. 2. MQ1-β crystal belongs to the triclinic system (Table S1 in Supporting information), presenting the three-dimension (3D) network with quadrangular voids (18.23 Å/14.54 Å). As the chlorine anchored in γ-position, IC-Cl-γ terminals impart the senior crystal system (monoclinic) and the 3D network with smaller voids (15.27 Å/10.87 Å) to MQ1-γ crystal. As shown in Figs. 2c and d, dramatic differences in intermolecular packing vertical to the "π-face-on" direction are observed. Owing to the highly twisted (D-A dihedral angle: 22.4°) conformers in MQ1-β, there is only four kinds of independent π-π interaction supporting the bent π-planes of MQ1-β molecules, including π-π interaction between end groups ("A-A" type: 3.41 Å) and π-π interaction between an end group and partially central π-core ("D-A" type: 3.37–3.47 Å). In contrast, the "brick-work" planes of MQ1-γ crystal are fabricated by more intense independent π-π interaction with shorter distances ("A-A" type: 3.40 Å; "D-A" type: 3.33–3.45 Å). Besides the "face-to-face" packing, the "edge-to-edge" intermolecular interactions are of equal importance in probing 3D networks. As shown in Figs. 2e and f, similar dimers linked by four pairs of CN···H hydrogen bonds (2.69–2.70 Å for MQ1-β and 2.67–2.80 Å for MQ1-γ) are both observed in the two acceptors. Nonetheless, the CN···H hydrogen bonds in MQ1-β incline to form clusters rather than the extended chain-like aggregation (Fig. S4 in Supporting information). Moreover, the other "edge-to-edge" interaction in MQ1-β (Cl···Cl: 3.35 Å) has no contribution in forming compact and ordered packing networks, thereby leading to the separated "CN···H" clusters (Fig. S4) and slack packing mode of MQ1-β. While the intense and multiform noncovalent interactions (CN···H: 2.47 Å, Cl···Cl: 3.43 Å, and Cl···H: 2.93 Å) exhibited in MQ1-γ all collaborate on the formation of highly interlocked packing motifs and chain-like J-aggregation (Fig. 2f and Fig. S5 in Supporting information). As expected, such a little modification on the

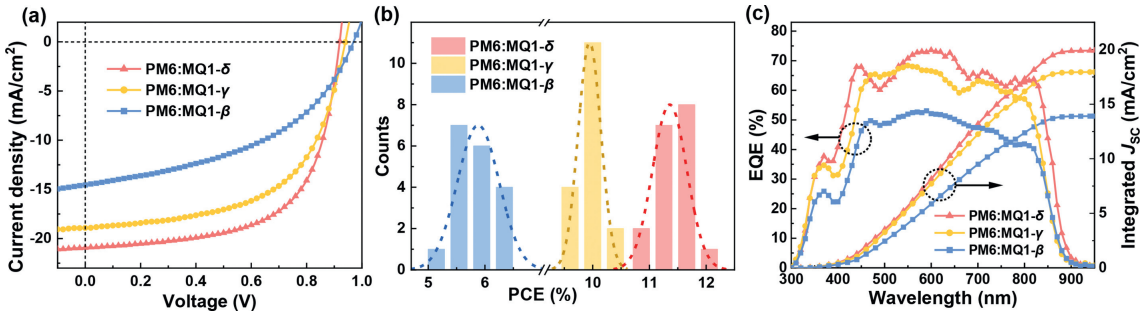

Fig. 3. (a) J-V plots, (b) PCE statistical distribution histograms, (c) EQE spectra and the corresponding integrated currents of the OSCs based on PM6:MQ1-δ, PM6:MQ1-γ, PM6:MQ1-β.

Table 2
Photovoltaic parameters of the optimal OSCs based on MQ1-δ, MQ1-γ, and MQ1-β.

Active layer	V_{OC} (V)[a]	J_{SC} (mA/cm^2)[b]	FF (%)[a]	PCE (%)[a]
PM6:MQ1-δ	0.912 (0.910 ± 0.002)	20.93 (19.91)	63.26 (62.32 ± 0.53)	12.08 (11.51 ± 0.18)
PM6:MQ1-γ	0.936 (0.935 ± 0.002)	18.90 (17.97)	57.96 (57.24 ± 0.45)	10.26 (10.00 ± 0.11)
PM6:MQ1-β	0.968 (0.963 ± 0.003)	14.54 (13.92)	45.93 (44.35 ± 0.70)	6.46 (6.02 ± 0.17)

[a] In parentheses are average values based on more than 10 devices.
[b] In parentheses are integrated J_{SC} values from the EQE spectra.

substitution position of chlorine on π-backbone affects both in the symmetry of crystal systems and packing motifs.

To evaluate the photovoltaic performance of the three isomeric acceptors, we fabricated the binary BHJ OSCs with a device structure of ITO/PEDOT:PSS/active layer/PDIN/Ag. The specific photovoltaic parameters of all optimized conditions such as D/A weight ratios (1:1), the volume amount of 1-chloronaphthalene (CN) additive (0.5 vol%), and thermal annealing temperatures (90 °C) were summarized in Tables S2-S4 (Supporting information). The current density-voltage (*J-V*) curves and the critical parameters including PCE, open-circuit voltage (V_{OC}), short-circuit current density (J_{SC}) and fill factor (FF) were presented in Fig. 3a and Table 2, respectively. Fig. 3b showed the histograms and corresponding Gaussian distribution of PCE counts for PM6:MQ1-β-, PM6:MQ1-γ-, and PM6:MQ1-δ-based devices. As chlorine changes from β-, to γ-, and to δ-position in the end groups of NFAs, the V_{OC} of related devices diminishes, while the J_{SC}, FF, and PCE of related devices increases, successively. In detail, the PM6:MQ1-β-based cell showed the highest V_{OC} of 0.968 V but the lowest PCE of 6.46% due to the inferior J_{SC} (14.54 mA/cm^2) and FF (45.93%). The PM6:MQ1-γ-based cell delivered a PCE of 10.26% accompanied by a V_{OC} of 0.936 V, a J_{SC} of 18.90 mA/cm^2, and an FF of 57.96%. The improved PCE of PM6:MQ1-γ-based device can be attributed to the efficient charge transport in the nanocrystalline zones of MQ1-γ. Furthermore, a PCE of 12.08% (V_{OC} = 0.912 V, J_{SC} = 20.93 mA/cm^2, FF = 63.26%) was recorded for the PM6:MQ1-δ-based device. Notably, the highest J_{SC} of the PM6:MQ1-δ-based device was mainly derived from its smallest bandgap among the three acceptors. As shown in the external quantum efficiency (EQE) spectra (Fig. 3c), the integrated J_{SC} of the PM6:MQ1-β-, PM6:MQ1-γ-, and PM6:MQ1-δ-based devices are calculated to 13.92, 17.97, and 19.91 mA/cm^2, respectively, in which the mismatches between the J_{SC} from the *J-V* measurements and the integrated J_{SC} from EQE spectra were all lower than 5%, indicating that the PCEs reported in this work are trustworthy.

Photoluminescence (PL) quenching experiments were employed to further probe the charge transfer behaviors of the blends based on these NFAs. As shown in Fig. S7 (Supporting information), the PL of PM6 was almost quenched by the acceptors in the blend films, and the PL of the three acceptors was also practically quenched by the PM6 donor. In detail, when excited at 780 nm, the three NFAs showed evident emission peaks of 868 nm for MQ1-γ, 879 nm for MQ1-δ, and 881 nm for MQ1-β, respectively. The quenching efficiency of 95.6% for MQ1-δ-based blend was higher than those of MQ1-β- (87.1%) and MQ1-γ-based (93.2%) counterparts, indicating the most efficient exciton dissociation and charge transfer between PM6 and MQ1-δ. To further investigate the exciton dissociation and charge extraction behavior of the three OSCs, the curves of photocurrent (J_{ph}) *versus* efficient voltage (V_{eff}) were plotted in Fig. S7. Based on the equation of $P_{dis} = J_{ph}/J_{sat}$, the exciton dissociation efficiency (P_{dis}) was applied to gage the inclination of exciton dissociation, in which J_{sat} is the saturation current density. As V_{eff} ascended, the J_{ph} reached saturation (J_{sat}) at a high V_{eff} (>2.0 V). The P_{dis} values were calculated as 74.4% for PM6:MQ1-β-, 91.5% for PM6:MQ1-γ-, and 92.6% for PM6:MQ1-δ-based devices, respectively. The higher the P_{dis} value is, the more efficient exciton and charge extraction in OSCs are. To probe the recombination behavior, the correlation between J_{SC} and light intensity (P_{light}), described as $J_{SC} \propto P_{light}^{\alpha}$, was established by recording the *J-V* curves under varied P_{light} values. Indicating the degree of bimolecular recombination, the α value near 1 indicates minimal or no bimolecular recombination in devices. The α values for PM6:MQ1-β-, PM6:MQ1-γ- and PM6:MQ1-δ-based devices were 0.984, 0.994, and 0.998, respectively, indicating that PM6:MQ1-δ-based device exhibits the weakest recombination among all the three isomeric acceptor-based devices thanks to the good miscibility between MQ1-δ and PM6. In all, the P_{dis} and α values for the three different OSCs follow the order of PM6:MQ1-δ > PM6:MQ1-γ > PM6:MQ1-β, which is consistent with their PCE variation.

To further investigate the difference in charge transport abilities of the three blend films, hole (μ_h) and electron (μ_e) mobilities were measured by the space-charge-limited-current (SCLC) method, and the related data were presented in Fig. S8 and Table S5 (Supporting information). PM6:MQ1-β-based devices had μ_h and μ_e values of 6.0×10^{-5} and 2.2×10^{-5} cm^2 V^{-1} s^{-1}, respectively, with a μ_h/μ_e ratio of 2.8. The most unbalanced μ_h and μ_e values for the PM6:MQ1-β-based blend are partly responsible for its lowest J_{SC}, FF, and PCE values, which are mainly derived from the high surface energy of MQ1-β and the poor miscibility of PM6 and MQ1-β. In contrast, PM6:MQ1-γ-based devices exhibited champion μ_h and μ_e values of 6.4×10^{-5} and 3.5×10^{-5} cm^2 V^{-1} s^{-1} among the three acceptor blends, which was ascribed not only to the interlocked π-π packing motif in the nanocrystal zone of MQ1-γ but also to the suitable interaction be-

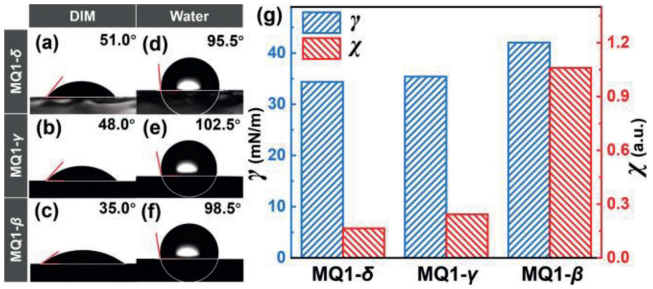

Fig. 4. The measured (a-c) DIM (diiodomethane) and (d-f) water contact angles of MQ1-δ, MQ1-γ, and MQ1-β. (g) Bar chart visualization of interfacial interaction analysis about surface energy (γ) and Flory-Huggins interaction parameter (χ) based on PM6:MQ1-δ, PM6:MQ1-γ, PM6:MQ1-β.

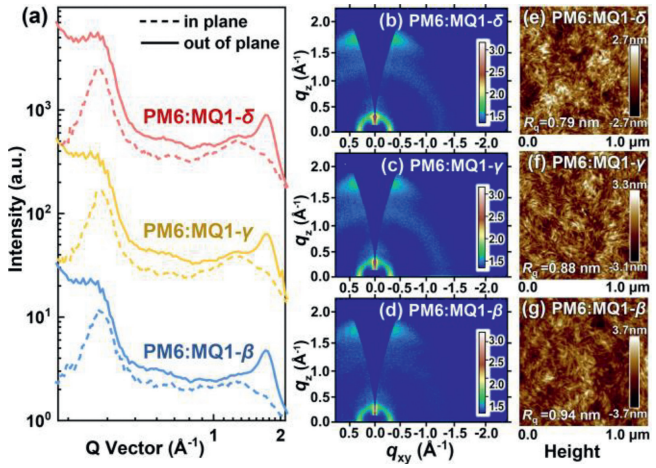

Fig. 5. (a) GIWAXS 1D linecuts in the out-of-plane and in-plane directions, (b-d) 2D GIWAXS patterns, (e-g) AFM height images of annealed blend films based on PM6:MQ1-δ, PM6:MQ1-γ, and PM6:MQ1-β.

tween the PM6 donor and MQ1-γ. Nonetheless, the μ_h/μ_e ratio of PM6:MQ1-γ blend (1.8) is higher than that of PM6:MQ1-δ blend (1.5), pointing to the imbalance of hole and electron transport in the PM6:MQ1-γ-based devices, thereby resulting in lower FF and J_{SC} values of PM6:MQ1-γ-based devices than MQ1-δ-based counterparts. Moreover, although the μ_e value (3.3×10^{-5} cm^2 V^{-1} s^{-1}) of MQ1-δ-based blend was slightly lower than the MQ1-γ-based counterpart, the lowest μ_h/μ_e ratio of PM6:MQ1-δ-based device guaranteed the most balanced charge transport thereby leading to the highest FF, J_{SC}, and PCE values among the three acceptors.

To get insight into the effect of substitution position of chlorine on the miscibility between the acceptor and donor (D/A miscibility), contact angle (CA) experiments of PM6 and the three isomeric acceptors were implemented with two solvents: diiodomethane (DIM) and deionized water. As shown in Fig. 4, the water (DIM) contact angles on the surfaces of MQ1-δ, MQ1-γ, and MQ1-β were 95.5° (51.0°), 102.5° (48.0°), and 98.5° (35.0°), respectively. Furthermore, the surface energy (γ) value of MQ1-β (42.04 mN/m) was remarkably higher than those of MQ1-γ (35.39 mN/m) and MQ1-δ (34.37 mN/m), which may be related to the inclination of self-aggregation of MQ1-β induced by the Cl···O interaction of IC-Cl-β. Moreover, the miscibility between PM6 and the three acceptors was gauged by Flory-Huggins interaction parameter (χ) that was calculated from the surface energies of donors and acceptors (Table S6 in Supporting information). In principle, the smaller the χ value is, the better the miscibility is, and *vice versa* [39]. As depicted in Fig. 4g, PM6:MQ1-δ-based blend exhibited the lowest χ value (0.165 K) among the three acceptors, indicating that homogenous BHJ blend may be obtained by the congenial interaction and impressive miscibility between PM6 and MQ1-δ. Besides, the slightly higher χ value of PM6:MQ1-γ (0.243 K) is also an indicator of suitable morphology of blend films. Compared to the PM6:MQ1-δ-based blend, the almost six-fold χ value of PM6:MQ1-β (1.06 K) represents the poorest D/A miscibility of MQ1-β among the three acceptors. Moreover, the undermixed morphology of the PM6:MQ1-β blend is detrimental to charge extraction and charge transport between donor and acceptors, thereby leading to the lowest J_{SC}, FF, and PCE of PM6:MQ1-β-based devices. In comparison, the excellent D/A miscibility between PM6 and MQ1-δ is beneficial for suitable morphology and less defect in their blends, which facilitate charge dissociation and transfer between the two domains.

To further probe the impact of D/A miscibility on molecular packing behaviors and crystalline inclination of NFAs in blend films, grazing incidence wide-angle X-ray scattering (GIWAXS) experiments were implemented. Two-dimensional (2D) GIWAXS patterns and related 1D linecuts in Fig. 5 demonstrated the blend films of three acceptors also showed evident (010) diffraction peaks ($q_z = 1.731$–1.742 Å^{-1}) in the out-of-plane (OOP) direction and (100) diffraction peaks ($q_{xy} = 0.305$–0.313 Å^{-1}) in the in-plane (IP) direction, respectively. The π-π stacking distances estimated from the (010) peaks decreased as the acceptor in blend film changed from MQ1-β (3.63 Å), to MQ1-γ (3.62 Å), and to MQ1-δ (3.61 Å). Notably, the trend of π-π stacking distances in blend film is consistent with that of pristine film (Table S7 in Supporting information), indicating the molecular aggregation behavior of the three acceptors was preserved in blend film. In the OOP direction, the crystal coherence lengths (CCLs) of pristine films/blend films were 27.8/19.9 Å for MQ1-β, 25.4/18.0 Å for MQ1-γ, and 28.6/18.4 Å for MQ1-δ, respectively. The biggest domain size of acceptors in MQ1-β-based blend film is mainly originated from its poor D/A miscibility. In comparison, the excellent miscibility of MQ1-δ and PM6 mitigates the strong crystallinity of MQ1-δ thereby leading to the suitable crystalline size and favorable morphology of PM6:MQ1-δ blends, matching with the improved charge-carrier mobility in the correlated BHJ film. Furthermore, atomic force microscopy (AFM) images in Figs. 5e–g demonstrated the fiber-like structure and conspicuous phase separation features in the blend films of the three acceptors The root-mean-square roughness (R_q) values of the three PM6-based blend films are successively elevated from 0.79 nm of MQ1-δ, to 0.88 nm of MQ1-γ, and to 0.94 nm of MQ1-β, in agreement with the trend of D/A miscibility of the three acceptors. The smallest R_q value of PM6:MQ1-δ-based blend indicates the smoothest surface which would lead to the favorable contact between active layer and interfacial layer thereby leading to efficient charge extraction.

In summary, we provided a facile yet effective approach to engineering molecular packing and miscibility of isomeric asymmetric NFAs in BHJ blends. The strong intramolecular Cl···O interaction derived from the IC-Cl-β end group induces the great surface energy and slack molecular packing of MQ1-β, as well as the undermixed BHJ blends with PM6, which impede the efficient charge transport thereby leading to the lowest J_{SC}, FF, and PCE of the MQ1-β-based devices. Owing to interlocked π-π packing and the better D/A miscibility of MQ1-γ, the PM6:MQ1-γ blend presented improved and more balanced mobility compared to PM6:MQ1-β-based counterparts, hence yielding the enhanced PCE of 10.26% of the resulting OSC devices. Finally, the strong crystallinity and compact molecular packing endowed by δ-chlorine substituted end groups for MQ1-δ lead to the most bathochromic absorption both in pristine and blend films. As a result, the PM6:MQ1-δ-based device presented the most balanced carrier transport and the highest PCE of 12.08%, which is supported by its superior D/A miscibility and shortest molecular packing distances. Overall, our investigation offers an in-

sight into the effect of monochlorinated terminals on molecular interaction, crystallinity, miscibility, and photovoltaic responds of NFAs.

Declaration of competing interest

The authors declare that they have no known competing financial interests or personal relationships that could have appeared to influence the work reported in this paper.

Acknowledgments

This work was supported by the National Natural Science Foundation of China (Nos. 52130306, 22075287, 22101285) and the Program of Youth Innovation Promotion Association CAS (No. 2021299).

Supplementary materials

Supplementary material associated with this article can be found, in the online version, at doi:10.1016/j.cclet.2023.108448.

References

[1] P. Cheng, G. Li, X.W. Zhan, Y. Yang, Nat. Photonics 12 (2018) 131–142.
[2] C.B. Nielsen, S. Holliday, H.Y. Chen, et al., Acc. Chem. Res. 48 (2015) 2803–2812.
[3] T. Ameri, P. Khoram, J. Min, C.J. Brabec, Adv. Mater. 25 (2013) 4245–4266.
[4] Y. Liu, B. Li, C.Q. Ma, et al., Sci. China Chem. 65 (2022) 224–268.
[5] C.Z. Sun, X. Lai, T. Rehman, et al., J. Mater. Chem. C 10 (2022) 17174–17181.
[6] S. Luo, F. Bai, J. Zhang, et al., Nano Energy 98 (2022) 107281.
[7] Y. Zhang, Y. Ji, Y. Zhang, et al., Adv. Funct. Mater. 32 (2022) 2205115.
[8] X. Yuan, Y. Zhao, D. Xie, et al., Joule 6 (2022) 647–661.
[9] H. Wang, H. Lu, Y.N. Chen, et al., Adv. Mater. 34 (2022) 2105483.
[10] W. Liu, J. Yuan, C. Zhu, et al., Sci. China Chem. 65 (2022) 1374–1382.
[11] R. Sun, Y. Wu, X. Yang, et al., Adv. Mater. 34 (2022) 2110147.
[12] L. Zhan, S. Li, Y. Li, et al., Joule 6 (2022) 662–675.
[13] L. Yang, H. Wang, J. Cao, et al., Chem. Eng. J. 427 (2022) 131942.
[14] Z. Bi, H.B. Naveed, H. Wu, et al., Adv. Energy Mater. 12 (2022) 2103735.
[15] K. Xian, S. Zhang, Y. Xu, et al., Sci. China Chem. 66 (2023) 202–215.
[16] X. Jiang, J. Yang, S. Karuthedath, et al., Angew. Chem. Int. Ed. 59 (2020) 21683–21692.
[17] Z. Zhou, W. Liu, G. Zhou, et al., Adv. Mater. 32 (2020) 1906324.
[18] Y. Lin, J. Wang, Z.G. Zhang, et al., Adv. Mater. 27 (2015) 1170.
[19] S.M. Swick, W. Zhu, M. Matta, et al., Proc. Natl. Acad. Sci. U. S. A. 115 (2018) E8341–E8348.
[20] X. Li, H. Huang, I. Angunawela, et al., Adv. Funct. Mater. 30 (2020) 1906855.
[21] Y.L. Ma, D.D. Cai, S. Wan, et al., Natl. Sci. Rev. 7 (2020) 1886–1895.
[22] C. Tang, X. Ma, J.Y. Wang, et al., Angew. Chem. Int. Ed. 60 (2021) 19314–19323.
[23] J. Yuan, Y.Q. Zhang, L.Y. Zhou, et al., Joule 3 (2019) 1140–1151.
[24] L. Zhu, M. Zhang, J. Xu, et al., Nat. Mater. 21 (2022) 656.
[25] D.H. Li, X. Zhang, D. Liu, T. Wang, J. Mater. Chem. A 8 (2020) 15607–15619.
[26] X. Liao, H. Pei, H. Zhao, et al., Chem. Eng. J. 435 (2022) 135020.
[27] J. Xu, F. Lin, L. Zhu, et al., Adv. Energy Mater. 12 (2022) 2201338.
[28] X. Wang, A. Tang, J. Yang, et al., Sci. China Chem. 63 (2020) 1666–1674.
[29] C. Yang, Q. An, H.R. Bai, et al., Angew. Chem. Int. Ed. 60 (2021) 19241–19252.
[30] H. Lu, H. Jin, H. Huang, et al., Adv. Funct. Mater. 31 (2021) 2103445.
[31] G. Han, T. Hu, Y. Yi, Adv. Mater. 32 (2020) 2000975.
[32] Q. Tu, W. Zheng, Y. Ma, et al., CCS Chem. 5 (2023) 455–468.
[33] S. Feng, M. Li, N. Tang, et al., ACS Appl. Mater. Interfaces 12 (2020) 4638–4648.
[34] Y. Pan, X. Zheng, J. Guo, et al., Adv. Funct. Mater. 32 (2022) 2108614.
[35] S.M. Swick, J.M. Alzola, V.K. Sangwan, et al., Adv. Energy Mater. 10 (2020) 2000635.
[36] S. Dai, F. Zhao, Q. Zhang, et al., J. Am. Chem. Soc. 139 (2017) 1336–1343.
[37] C. Yang, S. Zhang, J. Ren, et al., Chin. Chem. Lett. 32 (2021) 2274–2278.
[38] H.F. Yao, J.W. Wang, Y. Xu, et al., Acc. Chem. Res. 53 (2020) 822–832.
[39] L. Ye, H. Hu, M. Ghasemi, et al., Nat. Mater. 17 (2018) 253–260.